Enhanced Photocatalytic Performance of TiO2@CeO2 Hollow Structure through Synergetic Surface and Interface Engineering

Chun-hsien Lin, Yi-che Chen, Pei-kai Hsu, Alexandre Gloter, Wei-hsiang Huang, Chi-liang Chen, Jenn-ming Song, Shih-yun Chen

Hollow Structure through Synergetic Surface and Interface Engineering

Chun-Hsien Lin, Yi-Che Chen, Pei-Kai Hsu, Alexandre Gloter, Wei-Hsiang Huang, Chi-Liang Chen, Jenn-Ming Song, and Shih-Yun Chen**

In this study, a synergetic structural design is developed to improve the photocatalytic performance of the sub-micro core–shell hollow sphere (TiO_2@H-CeO_2). TiO_2@H-CeO_2 with maximum surface/interface effect is chosen as the substrate and then reacts with different concentrations of $Ce(NO_3)_3 \cdot 6H_2O$ solutions. Optical properties analysis shows that after the reaction, the band gap of the composite structure and the electron–hole recombination efficiency both decrease while the photodegradation ability is effectively improved. Spectroscopic and microscopic observations reveal two changes in the structure after the reaction. The first is the deposition of CeO_2 nanoparticles that can be observed inside and on the surface of the shell; the second is the doping of Ce^{3+} in the TiO_2 nanoparticles of this shell. The deposition of CeO_2 particles increases the interfacial area between the CeO_2 and TiO_2 and facilitates the corresponding charge transfer. The Ce^{3+} doping in the TiO_2 shell changes the optical properties of TiO_2. Therefore, the improved performance of the composite structure can be attributed to the synergy of different surfaces and interfacial effects caused by the reactions.

1. Introduction

Owing to environmental protection awareness and the energy crisis, the development of scarce and sustainable strategies for Physiochemical processes has attracted more and more attention. The photocatalyst is one of the promising materials that could fulfill the requirements because it only needs light as the driving source; it can carry out redox reactions to decompose the surrounding organic molecules, resulting in sterilization and self-cleaning, deodorization, and even generate energy such as hydrogen. Besides, the energy loss in the photodegradation reaction process is low and does not produce toxic substances.

TiO_2 is one of the most attractive photocatalysts. Since Fujishima and Honda[1] discovered that it could decompose water into oxygen and hydrogen under ultraviolet light irradiation in the 1970s, many researchers have invested in related studies. However, pristine TiO_2 is catalytic only under ultraviolet light. In the solar spectrum,the proportionof ultraviolet lightisonlyabout5%,whiletherestismainlyvisiblelight,≈50%. Thus, it is necessary to improve the catalytic ability of TiO_2 under the visible light region. Up to now, various methods have been utilized, such as doping metal or non-metal ions,[2,3] changing the morphology to increase the surface area,[4,5] and forming heterojunctions.[6–8] On the other hand, photocatalyst materials with sub-micro core–shell structures have also attracted extensive research,[9,10] which could avoid some disadvantages, including thermal instability,[11] dissolvability in solution,[12] and toxicity as it appears at the scale of only a few nanometers.[13]

C.-H. Lin, Y.-C. Chen, P.-K. Hsu, S.-Y. Chen
Department of Materials Science and Engineering
National Taiwan University of Science and Technology
Taipei 106335, Taiwan
E-mail:sychen@mail.ntust.edu.tw
A.Gloter
LaboratoiredePhysiquedesSolides
CNRS
UniversitéParis-Saclay
Orsay91405,France
E-mail:alexandre.gloter@u-psud.fr
W.-H.Huang,C.-L.Chen
NationalSynchrotronRadiationResearchCenter
Hsinchu30076,Taiwan
J.-M.Song
DepartmentofMaterialsScienceandEngineering
NationalChungHsingUniversity
TaichungTaiwan

Different materials have been utilized to form core–shell structure composite with TiO_2, for instance, CeO_2-TiO_2,[14] ZnO-TiO_2,[15] Sm_2O_3-TiO_2,[16] and MnO_2-TiO_2.[17] Among them, the Ce-based photocatalyst has gained popularity. CeO_2 is highly capable of remedying indoor pollutants based on the reversible shifting between Ce^{3+} and Ce^{4+} oxidation states.[18] In addition, it shows high chemical stability and large oxygen storage capacity. Up to now, various synthetic routes have been used to obtain TiO_2-CeO_2-based composites with different structural designs.[19–23] The enhanced photocatalytic performance was attributed to the induced interfacial interactions, which extend the absorption range to the visible light region, prolong the lifetime of electron–hole pairs, and reduce the recombination probability. Recently, a facile two-step method was developed to prepare TiO_2@H-CeO_2 submicron hollow composites with promising photocatalytic properties.[24] The hollow structure is featured by its low density and high surface area, providing more active sites at the surface. However, the efficiency was limited by the relatively limited amount of interfacial area in these TiO_2@H-CeO_2 composites.

In this study, a simple surface treatment process is taken place to modify the microstructure of the outer TiO_2 shell of TiO_2@HCeO_2 composites. TiO_2@H-CeO_2 composite with optimum photocatalytic performance was used as the substrate and then dispersed in $Ce(NO_3)_3{\cdot}6H_2O$ solution with different concentrations. An improved photodegradation ability was obtained under either UV or visible light by using methylene blue (MB) as the dye. The rate constant K was enhanced to 0.11 and 0.03 min^{-1} under UV and visible light, respectively. The photocatalytic performance is discussed for the changes in the TiO_2 shell structure observed by various spectroscopic and microscopic techniques.

2. Results and Discussion

2.1. Photocatalytic Performance

Figure 1a demonstrates the photodegradation results under visible light irradiation. Negligible catalytic activity was observed in bare TiO_2 NPs and H-CeO_2. The formation of core–shell structure (Ti@Ce) improves the ability obviously. The photocatalytic performance was further enhanced with the $Ce(NO_3)_3{\cdot}6H_2O$ treatment. An optimum is obtained for sample 0.5Ce-Ti@Ce, where 80% of MB can be degraded in 60 min. The degradation efficiency is higher than the reported TiO_2-CeO_2 mesoporous composites (80% in 2 h),[25] zeolite-supported CdS/TiO_2/CeO_2 (75% in 60 min),[26] and even comparable with optimized CeO_2/TiO_2– NTs (94% in 60 min).[27] The photodegradation efficiency under UV light is plotted in Figure 1b. As expected, the bare TiO_2 NPs have there a non-negligible catalytic activity. Nevertheless, the Ti@Ce composites have a more robust photocatalytic ability, further enhanced after reacting with $Ce(NO_3)_3{\cdot}6H_2O$ solution. In sample 0.5Ce-Ti@Ce, almost 100% of MB can be degraded in 10 min. The degradation efficiency is higher than the yolk–shell structure of TiO_2@H-CeO_2 (60% in 10 min).[28] However, the efficiency did not change with increasing the Ce/Ti ratio to 0.9.

The variation of photocatalytic performance among the composites isquantifiedbycomparingtherateconstant K(Figure1c), which is estimated by fitting a pseudo-first-order kinetic model (Figure S3, Supporting Information). It is seen that the variation trend of the *K* value with the Ce/Ti ratio is similar either under visible or UV light. The value of K first increases gradually with the Ce/Ti ratio. The maximum *K* value was obtained in sample 0.5Ce-Ti@Ce. It decreased with further increasing the Ce/Ti ratio to 0.9. The *K* value of sample 0.5Ce-Ti@Ce reaches 0.03 and 0.11 min^{-1} under visible and UV light, respectively.

2.2. Optical Properties

The optical properties of the Ce-Ti@Ce composites were investigated by UV–vis absorption spectroscopy, and the results are shown in **Figure 2**a. It can be observed that the peak position of

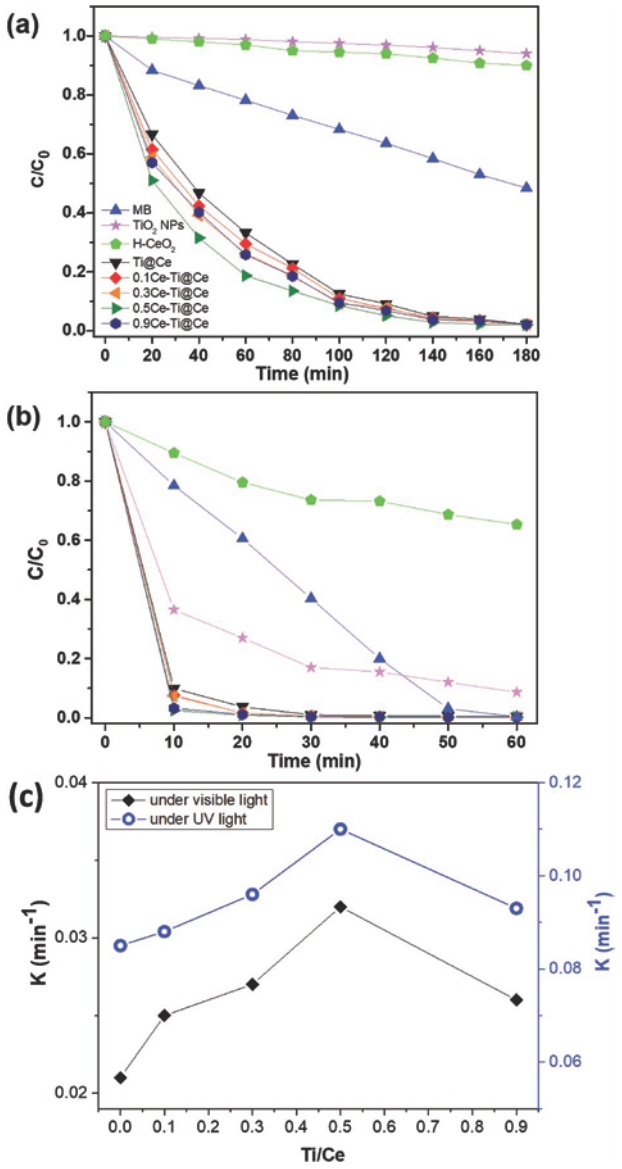

Figure 1. Photocatalytic performances of TiO_2 NPs, H-CeO_2 and CeTi@Ce composites under a) visible light and b) UV light. c) Rate constant *K* under UV light and visible light.

the composites shifts to the long wavelength side, and the absorption range expands as compared to that of sample Ti@Ce. The broadest absorption band was obtained in sample 0.5Ce-Ti@Ce, whose absorption range exceeds 500 nm. The band gap values for different samples estimated by analyzing the Tauc plots are plotted in the inset. The estimated band gap of bare TiO_2 NPs and $HCeO_2$ is 3.25 and 3.14 eV, respectively. The formation of the core– shell structure narrows the band gap to 3.05 eV, which has been attributed to the reduction of ceria at interfaces. After the reaction with $Ce(NO_3)_3{\cdot}6H_2O$ solution, the gap narrows down gradually. The smallest bandgap value among the Ce-Ti@Ce composites was obtained in sample 0.5Ce-Ti@Ce, ≈2.85 eV. The band gap value's narrowing is consistent with the enhanced photocatalytic performance under visible light.

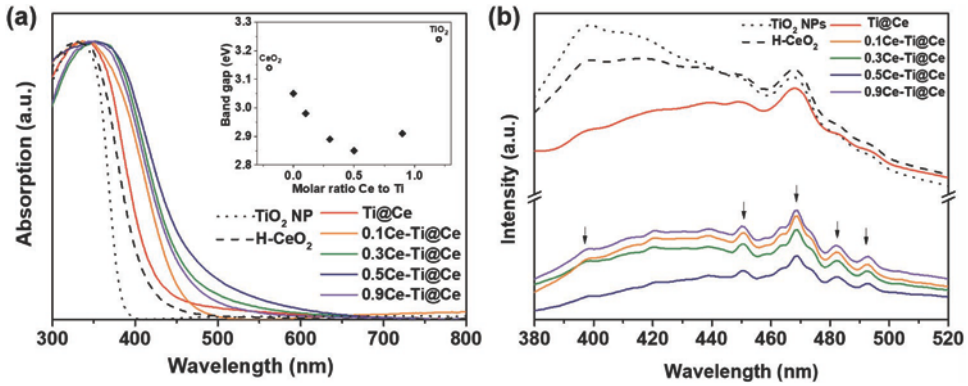

Figure 2. a) UV–vis spectrum for Ti@Ce and Ce-Ti@Ce composites and their band gap value (inset). b) PL spectrum for TiO_2 NPs, H-CeO_2, and Ti@Ce
and Ce-Ti@Ce composites.

The photoluminsence (PL) spectrum analysis was utilized to investigate the separation efficiency of photo-generated electrons and holes. Figure 2b shows the photoluminescence spectra recorded for the catalyst at 320 nm excitation wavelengths. The PL emission of bare TiO_2 NPs, H-CeO_2, Ti@Ce, and all CeTi@Ce composites was shown together. It shows that almost all the Ce-Ti@Ce composites had the same luminescence centers around 397, 452, 470, 482, and 492 nm. The peak at ≈400 nm was attributed to the emission of bandgap transition with the energy close to the bandgap energy of anatase (3.2 eV). The peaks at 452 and 470 nm are due to the surface states and oxygen vacancies of TiO_2, respectively.[29–31] The peak at 482 nm is characteristic of the Ce^{3+} state. In the present study, it is observed that all Ce-Ti@Ce composites exhibit almost identical emission bands, indicating that these samples have the similar defect structure.

Next, it is noted that as compared with sample Ti@Ce, the PL intensity of all Ce-Ti@Ce composites decreased significantly, indicating that the reaction with $Ce(NO_3)_3{\cdot}6H_2O$ solution promotes the charge separation efficiency and inhibits the recombination of photo-generated electrons and holes under light illumination. Among the Ce-Ti@Ce composites, the PL intensity decreased with the increase of the Ce/Ti ratio and reached a minimum when the ratio was 0.5. However, the intensity of PL increased when the Ce/Ti ratio was increased further. The intensity decline generally indicates that the recombination of photogenerated electrons and holes was inhibited, resulting in higher photocatalytic activity. The PL results were consistent with the photocatalytic performance of the Ti@Ce and all Ce-Ti@Ce composites.

2.3. Microstructure of Ceo_2@Tio_2@H-Ceo_2 Hollow Core–Shell Composites

The microstructure of the composites was determined first by Xray diffraction analysis (XRD). **Figure 3**a shows the XRD pattern of the sample Ti@Ce along with the ones of the samples 0.1CeTi@Ce, 0.3Ce-Ti@Ce, 0.5Ce-Ti@Ce, and 0.9Ce-Ti@Ce. In these spectra, all the peaks correspond to CeO_2 (JCPDS 34-0394) and TiO_2 (JCPDS 21-1272). No other crystalline phases were found. The intensity ratio between peaks from TiO_2 and CeO_2 decreases after the reaction with $Ce(NO_3)_3$. $6H_2O$ solution, indicating the

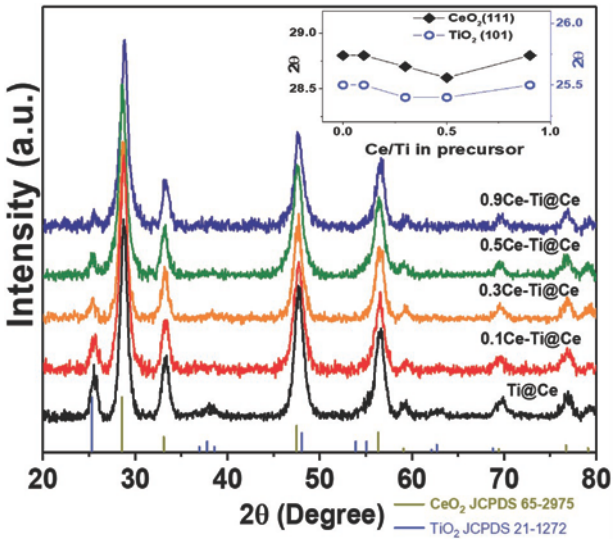

Figure 3. XRD pattern of the sample Ti@Ce along with the ones of the samples 0.1Ce-Ti@Ce, 0.3Ce-Ti@Ce, 0.5Ce-Ti@Ce,and0.9Ce-Ti@Ce. The peak shift of TiO_2 (101) and CeO_2 (111) with Ce/Ti ratio is shown in the inset figure.

formation of additional ceria. TiO_2 (101) and CeO_2 (111) peaks revealed a shift for both phases. The relation between the peak position and Ce/Ti ratio is shown in the inset figure.

Both the TiO_2 (101) and CeO_2 (111) peak shift to a lower angle gradually until the Ce/Ti ratio reaches 0.5. In sample 0.9Ce-Ti@Ce, both shifts are negligible as compared to the Ti@Ce. The shift to a lower angle implies the increased spacing in the TiO_2 (101) and CeO_2 (111) planes. These behaviors first indicate that the extra ceria is more reduced than the hollow ceria in the 0.1Ce-Ti@Ce to 0.5Ce-Ti@Ce samples. In addition, the lattice expansion of TiO_2 demonstrates that the structure of the titania shell also undergoes some chemical changes during the reaction. With further deposition, the ceria shows a peak position similar to the hollow ceria core.

The valence state changes of Ti and Ce in each sample were analyzed by X-ray absorption spectrum (XAS). **Figure 4**a is the Ce-*L* edge X-ray absorption near-edge structure (XANES) of each sample, which is contributed by the transition of $2p_{3/2} \rightarrow 5d$. After subtracting the background of an arctan function, each spectrum was fitted with five Gaussian functions. The five peaks represent different transition processes. Peaks A_1 and A_2 come from Ce^{4+} (with a final state $2p^5 4f^0 5d^*$ where d^* means that there is an excited electron in the 5d orbital), peak B also originates from Ce^{4+} (but with a final state $2p^5 4f^1 5d^* \underline{L}$ where $\underline{L}$ means a hole generated in the oxygen *p* orbital), peak C is related to Ce^{3+} (with a final state $2p^5 4f^1 5d^*$). Peak D is caused by the transition of $2p \rightarrow 4f$. A shoulder at ≈5727 eV is observed in all the spectra, indicating the presence of Ce^{3+} in the sample. The content of Ce^{3+} in the sample can be estimated from the proportion of the peak C area to the overall area, and the results are shown in the inset figure. It shows that the reaction with $Ce(NO_3)_3 \cdot 6H_2O$ solution will increase the overall Ce^{3+} content of the sample. The highest Ce^{3+} content is obtained in sample 0.5Ce-Ti@Ce, which is increased from 10% to 12%. The content of Ce^{3+} began to decrease with a further increase in the Ce/Ti ratio in the precursor.

Figure 4b is the Ti K-edge XANES of all samples, which can be used to determine information about the Ti4+ coordination environment in oxide materials.[32–35] The spectrum between 4965 and 4975 eV is primarily formed by the excitations of electrons from the 1s ground state to the 3d unoccupied states. The spectrum can be fitted by four peaks, as shown in the inset Figure (i). The A1 characteristic peak arises mainly from the dipole transition from 1s to p-3d(t2g) states (i.e., empty p states of the Ti absorber hybridized with empty Ti-3d states with t2g character) and from a contribution from quadrupole transitions from 1s to 3d(t2g). The relatively strong intensity of the A1 peak in these composites confirms that the local environment of the Ti is typical from an anatase structure, e.g., as compared to the case of rutile. Indeed, in the case of rutile, the A1 peak intensity is strongly reduced by the absence of 1s to p-3d(t2g) states transition due to the centrosymmetric at the Ti absorber site.[32] At the highest energy, peak B has been attributed to the dipole transitions from the 1s orbital to 3d(eg) states (either through hybridization with local Ti-4p orbital or via the p orbital of the ligand[33,35]). At intermediates energies, the A2-A3 peaks have been reported as a primary mixture of dipole transitions involving both 3d(t2g) and 3d(eg) orbitals with a minor contribution from quadrupole excitations with

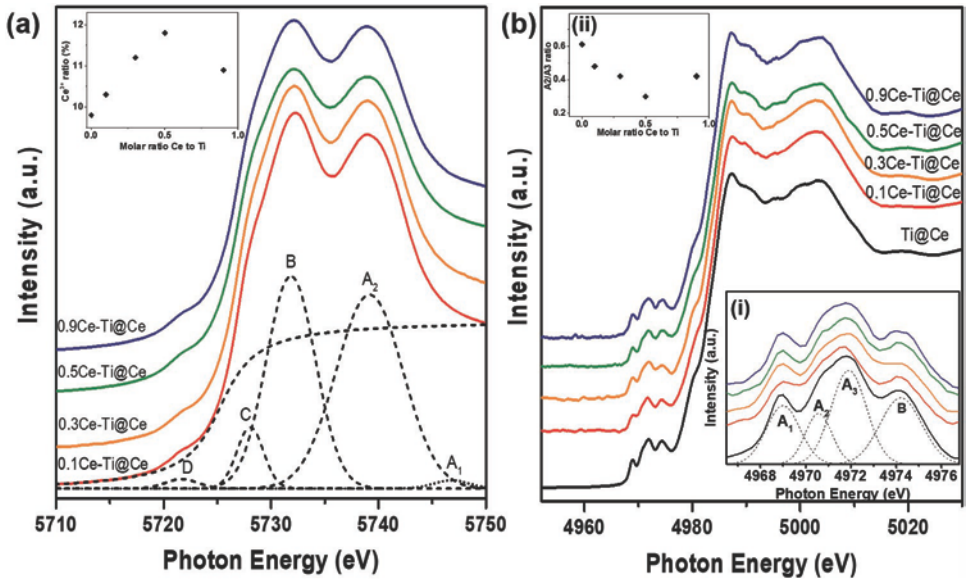

Figure 4. XANES spectrum of Ce-Ti@Ce composite structure with different Ce/Ti ratio. a) Ce L_3-edge. Ce^{3+} ratio obtained from the Ce L_3-edge was shown in the inset. b) Ti-*K* edge. Pre-edge and the A_2/A_3 ratio of each sample was demonstrated in the inset (i) and (ii), respectively.

3d(eg) final character.[32,34–36] Empirically, it has been reported that A2 peak may arise predominantly from the surface structure of the anatase particles and/or from Ti species associated with the surface.[37] The increase of the intensity ratio of the two peaks (A2/A3) has then been associated with the increase of five-coordinated titanium,[38] instead in accordance with the correlation between the coordination numbers of Ti sites with the pre-edge peak positions reported by Farges et al.[33] This figure shows thatpre-edgefeatureschangedslightlyastheratioofCe/Ti in the precursor increased. After minor dampening for the 0.1CeTi@Ce, the A1 peaks become more visible with additional ceria. A slight decrease in the peak ratio between A2 and A3 is also obtained (see inset Figure (ii) in Figure 4b). It may indicate a slight change in the local environment around the Ti absorbent, which can typically account for changes at the anatase surface when additional ceria interacts with the titania particles of the shell (e.g., less oxygen vacancy and/or some coverage by ceria adsorption).

Figure 5a–c shows the trasmission electron microscopy (TEM) investigations of samples 0.1Ce-Ti@Ce, 0.3Ce-Ti@Ce, and 0.9Ce-Ti@Ce, respectively. A shell made of nanoparticles is observed on the hollow sphere surface in all samples, and the shellthicknessvariesfrom20to60nm.HighresolutionTEMimage investigation of sample 0.3Ce-Ti@Ce is shown in Figure 5d, where particles with lattice fringes can be seen. Figures 5e,f are the fast Fourier transform (FFT) analysis of sample shell 0.3CeTi@Ce and 0.9Ce-Ti@Ce, respectively. As expected for the shell, diffraction rings with distances corresponding to the anatase structure are observed. The diffraction spots of CeO_2 also indicate the existence of CeO_2 phase inside the shell. Furthermore, it is found that the diffraction spots of CeO_2 phase are more evident in sample 0.9Ce-Ti@Ce than those in sample 0.3Ce-Ti@Ce. The

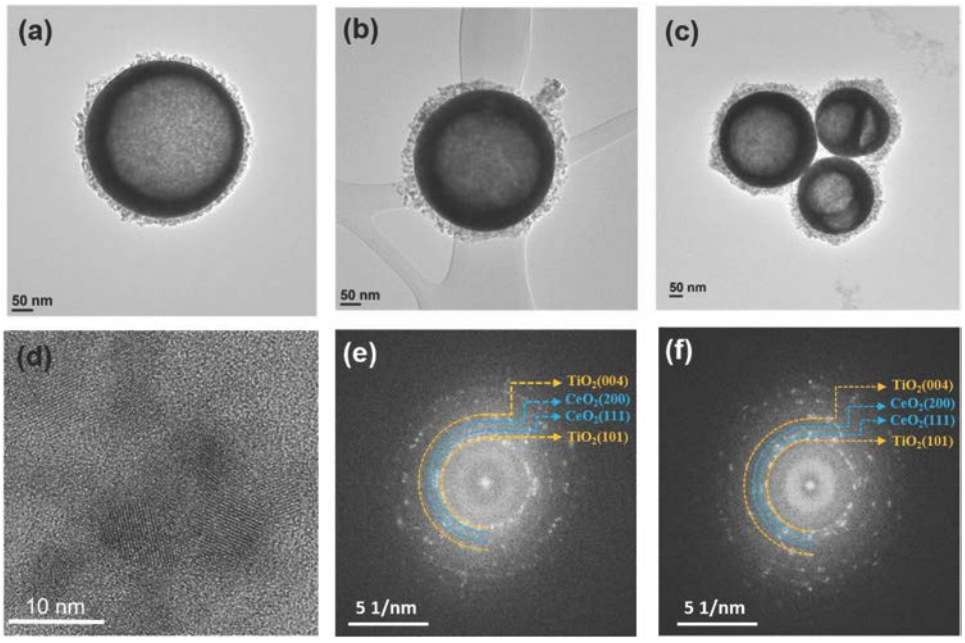

Figure 5. TEM images of Ce-Ti@Ce composite with different Ce/Ti ratio, a) 0.1Ce-Ti@Ce, b) 0.3Ce-Ti@Ce, and c) 0.9Ce-Ti@Ce. d) High resolution TEM image investigation of sample 0.3Ce-Ti@Ce. e,f) The FFT analysis of sample shell 0.3Ce-Ti@Ce and 0.9Ce-Ti@Ce, respectively.

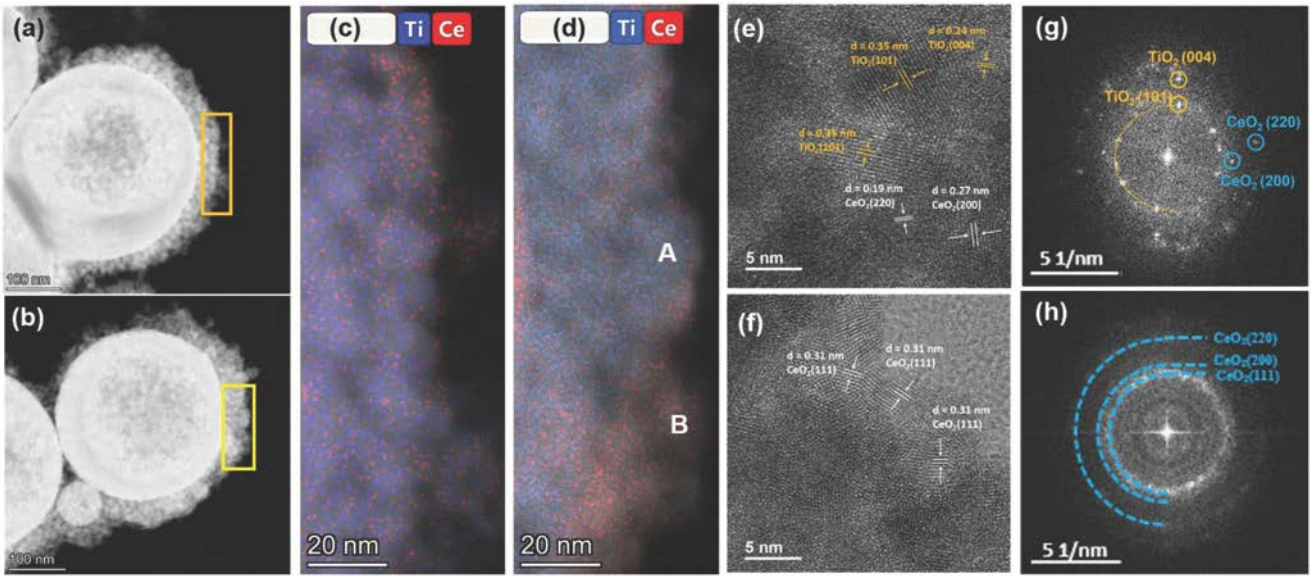

Figure 6. a,b) HAADF image of sample 0.3Ce-Ti@Ce and 0.9Ce-Ti@Ce, respectively. c,d) Elemental mapping of Ce and Ti of the yellow box 1 and 2. e,f) High resolution TEM images obtained from region A and B are shown, and g,h) the correlated FFT analysis is shown.

above results predict that the number of CeO_2 particles inside the TiO_2 shell increases with the Ce/Ti ratio in the precursor.

Energy disperive spectrum (EDS) was then utilized to reveal the distribution of elements of the Ce-Ti@Ce composites. **Figure 6**a,b shows the high angle annular dark field (HAADF) image of sample 0.3Ce-Ti@Ce and 0.9Ce-Ti@Ce, respectively. Elemental mapping of Ce and Ti of the shell was carried out in the marked regions. In sample 0.3Ce-Ti@Ce, slight Ce distributes homogeneously throughout the shell (Figure 6c).

The concentration of Ce ranges from 0.7 to 2 at% based on EDS analysis. On the other hand, in sample 0.9Ce-Ti@Ce, the distribution of Ce is inhomogeneous (Figure 6d). The concentration of Ce ranges from 1 at% (region A) to 14 at%

(region B). High resolution TEM images of these two regions are in Figure 6e,f. All the particles are crystallized. More particles can be assigned to CeO_2 in the shell of sample 0.9Ce-Ti@Ce. FFT analysis correlated to the shell is shown in Figure 6g,h. Region A mainly contributed to TiO_2 phase, and region B contains

of the shell contains only Ce and O, and the thickness of such a Ce-rich layer is of few nanometers.

EELS spectral structures of Ce, Ti, and O of five typical regions are investigated (Figure 7e–g). Area 1, 2, 3, 4, and 5 presents the outmost surface layer of the shell, the interior region of the TiO_2 shell, the interface layer in the TiO_2 shell

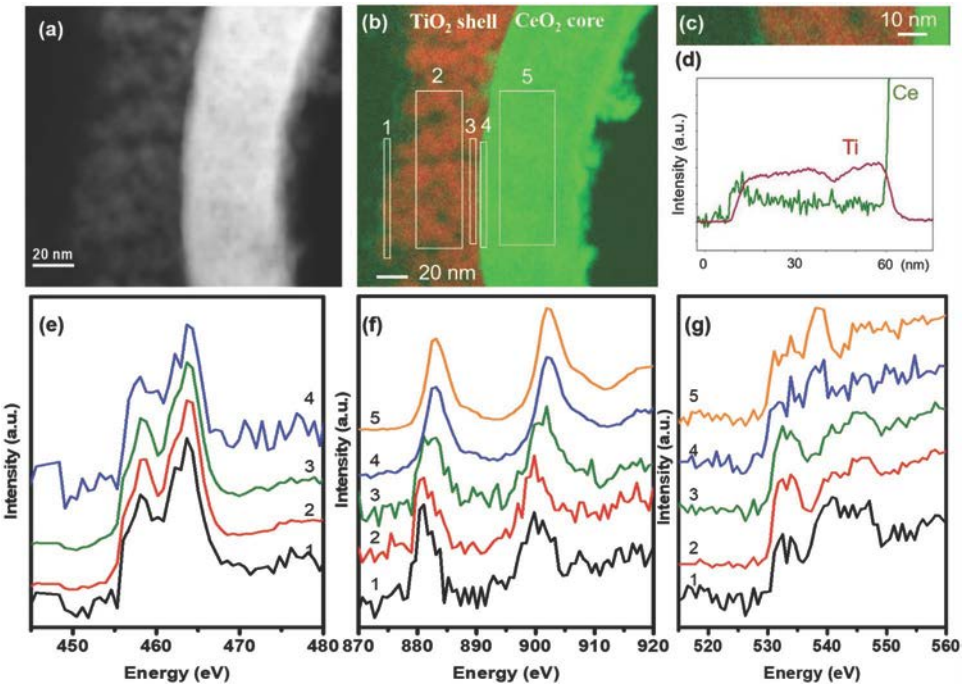

Figure 7. a) HAADF image of sample 0.3CeTiCe. b) Intensity of the EELS Ti-L and Ce-*M* edges. c) Zoom on an EELS mapping across the titania nanoparticles shell. d) The corresponding intensity profile of Ce and Ti is plotted together. e–g) EELS Ti-*L*, Ce-*M*, and O-*K* edges extracted from the white boxes are shown.

diffraction spots from CeO_2 phase clearly. Notably, aggregations of nanoparticles outside the composites were observed in sample 0.9Ce-Ti@Ce, as demonstrated in Figure S4 (Supporting Information). These clusters are not attached to the hollow spheres. According to diffraction analysis, the phase of these particles is found to be TiO_2 or a mixture of CeO_2 and TiO_2. Notably, a small amount of Ce was detected in the TiO_2 particles.

The chemical distribution and valence state of elements in the sample was analyzed by electron energy loss spectrum (EELS) with high spatial resolution. **Figure 7**a is the HAADF image of sample 0.3CeTiCe. The mapping results of the Ce M edge and Ti L edge of the composite is demonstrated in Figure 7b. A small amount of Ce was detected throughout the TiO_2 shell, consistent with the above EDS analysis. It is worth noting that a thin Cerich layer appears on the surface of the TiO_2 shell (Figure 7c). As revealed by the line profile (Figure 7d), the outermost surface side, the interface layer in the CeO_2 shell side, and the interior region of CeO_2 hollow core. Qualitatively, Ce *M*-edges and Ti *L*-edges can indicate valence evolution by observing their energy shifts and shapes. In the case of the Ce-*M* (Figure 7f), an intense edge is measured in the hollow core with a primary Ce^{4+} redox state. Energy shifts to lower energy are observed for the other areas indicating more reduced ceria, already starting at the interface of the hollow sphere with the titania shell (spectra 3). At the extremity of the very thin shell, the surface exhibits a much narrow Ce-M_5 line located at lower energy, at ≈880 eV, indicating a primary Ce^{3+} redox. Within the TiO_2 shell, a rather diluted Ce spectral signature is measured and spectrum 2, while integrated over a relatively large area, is still noisy. Nevertheless, it evidences a mixed Ce redox state. The EELS Ti-*L* edges have low energy resolution, but it indicates a slight reduction of the titania redox state next to the interface with the CeO_2 hollow cores and the outmost layer. The O-*K* edges are more representative of the ceria (area 4–5) and titania (area 1–3) and confirm some trends from the Ce-*M* edges. Indeed, the

O-*K* pre-edge for spectrum 1 is weaker, confirming a lower redox state of the anatase at the surface.

Figure 8 is the schematic figure showing the structural changes of TiO_2@H-CeO_2 hollow sphere composites after reacting with different concentrations of $Ce(NO_3)_3 \cdot 6H_2O$ solutions. First, TiO_2@H-CeO_2 hollow sphere was obtained by the deposition of TiO_2 nanoparticles on the surface of the annealed CeO_2 hollow spheres. In such a two-layered structure, the interface region is Ce^{3+}-rich, while the surface of the TiO_2 layer is Ti^{3+}rich.[24] The reaction with low concentration $Ce(NO_3)_3 \cdot 6H_2O$ solution results in the Ce^{3+} doping into the TiO_2 shell and ceria adsorptiononthesurface(typeI).Achangeinthecrystallinityoft he TiO_2, as observed by XRD and different XAS signatures probed on the Ti absorber, both indicate changes in the Ti─O bonding associated with the functionalization with the ceria. With enhancingtheconcentrationof$Ce(NO_3)_3 \cdot 6H_2O$solution,CeO_2 nanoparticles formed (type II). Further increasing the content of Ce in the precursor, the amount of CeO_2 nanoparticles in the shell increased and even formed CeO_2 clusters (type III). However, the concentration of Ce in the TiO_2 NPs did not increase, obviously.

Notably, the formation of CeO_2 nanoparticles inside the TiO_2 shell results in the reduced cerium valence and then contribute to a direct photocatalytic behavior of CeO_2, i.e., under the visible light region. Furthermore, it increases the TiO_2/CeO_2 interface area and the charge reconstruction and, in a general way, modifies the surface of the titania nanoparticle, which is known to increase the photocatalytic activity through band bending.[39] On the other hand, the Ce^{3+} doping in the TiO_2 nanoparticles, which is confirmed by the structural modification of the TiO_2 concomitant with the observation of EDS and EELS weak signal of ceria wherever within the shell, is known to result in enhanced catalytic performance due to the formation of Ce 4*f* and oxygen defect levels beneath the conduction band minimum. Band gap of TiO_2 down to ≈3 eV was reported solely by ceria doping.[40]

Consequently, the influence of Ce/Ti ratio on the photocatalytic performance of Ce-Ti@Ce composite can be interpreted. As the Ce/Ti ratio raised from 0 to 0.5, both the CeO_2 nanoparticles amount formed inside the TiO_2 shell and the Ce^{3+} doping level into the TiO_2 particles increased, which reduced the band gap and suppress the electron–hole recombination rate and thus enhanced photocatalytic performance. With further enhancing the Ce/Ti ratio to higher than 0.5, the growth of CeO_2 nanoparticles from adsorbed atoms or ultrasmall clusters at the surface result in a particle with less Ce^{3+} with wider band gap and benefit to the recombination. Therefore, the photocatalytic performance declines. In the present study, the best performance is obtained in sample 0.5Ce-Ti@Ce, which can be attributed to the synergetic effects of TiO_2/CeO_2 interface interaction and Ce^{3+} doping and adsorption, the bang gap is as low as 2.85 eV.

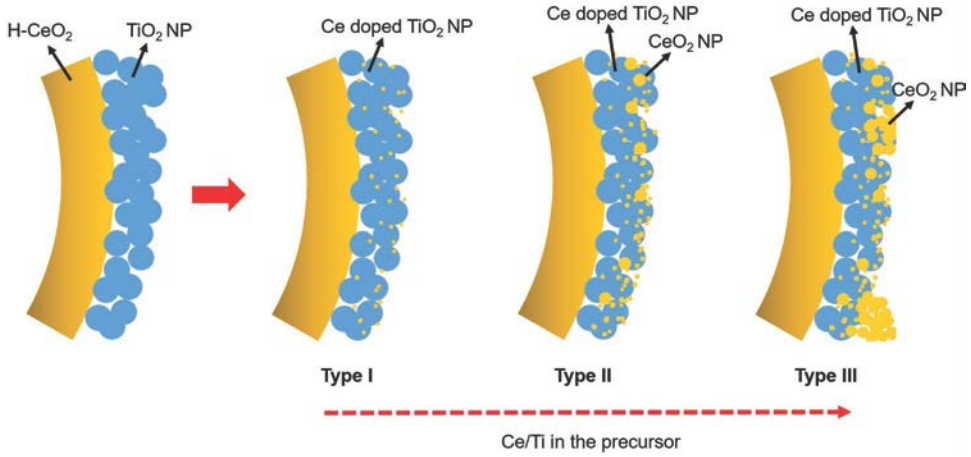

Figure 8. The schematic diagram of the structural changes of TiO_2@H-CeO_2 hollow sphere composites after reacting with different concentrations of $Ce(NO_3)_3 \cdot 6H_2O$ solutions.

3. Conclusion

The present study reveals the promotion effect of $Ce(NO_3)_3 \cdot 6H_2O$-treatment on TiO_2@H-CeO_2 composites photocatalytic degradation of MB under visible and UV light. Our results demonstrate that Ce doping and CeO_2 formation occur during the reaction. The doped Ce introduces a new electronic level close to the conducting band, facilitating the separation of charge carriers, inhibiting their recombination,

reducing the band gap, and shifting the light absorption to the visible range.

4. Experimental Section

Preparation of TiO_2@H-CeO_2: At first, CeO_2 hollow spheres (H-CeO_2) were prepared using a spray pyrolysis (SP) method. The detailed synthesis process has been previously described.[41] The obtained H-CeO_2 was annealed in air at 300 °C for 2 h. The annealed H-CeO_2 was dispersed in isopropanol, then a solution containing titanium isopropoxide (TTIP, 97%, Sigma Aldrich) and anhydrous alcohol (C_2H_5OH, 99.8%, Honeywell). The molar ratio between Ti and Ce varied from 0.5 to 3 by changing the amount of TTIP. After stirring for 2 h, deionized water mixed with ethanol was dropped into the above solution and stirred for another 24 h. The light yellow precipitate was washed with deionized water and ethanol and dried at 80 °C overnight. After annealing under 450 °C for 2 h, TiO_2@H-CeO_2 composites with different Ti/Ce ratio was obtained. The phase determination of the TiO_2@H-CeO_2 composites was studied by XRD. As shown in Figure S1 (Supporting Information), with increasing the ratio of Ti/Ce, the characteristic peaks of anatase TiO_2 grow rapidly. Next, the morphology was investigated by TEM. As demonstrated in Figure S2 (Supporting Information), nanoparticles deposit randomly on the hollow sphere surface as the ratio of Ti/Ce is 0.5. With increasing the ratio of Ti/Ce to 1, nanoparticles cover the whole sphere surface to become a core–shell structure. The shell becomes thick and rough as the ratio of Ti/Ce reaches 3.

Preparation of Ce-TiO_2@H-CeO_2: Then the TiO_2@H-CeO_2 composite with a Ti/Ce ratio of 2 (named sample Ti@Ce hereafter) was chosen as the substrate for further functionalization. At first, this Ti@Ce has dispersed in Cerium (III) nitrate hexahydrate ($Ce(NO_3)_3{\cdot}6H_2O$, 99.5%, Alfa Aesar) solution with different concentrations for 30 min. Then ammonia solution (NH_4OH, NH_3 content 28%, J. T. Baker) was dropped into the solution to adjust the pH value to 9–10. After reacting for 24 h, the mixture was centrifuged and dried. The obtained composites were named as 0.1CeTi@Ce, 0.3Ce-Ti@Ce, 0.5Ce-Ti@Ce, and 0.9Ce-Ti@Ce according to the molar ratio between the $Ce(NO_3)_3{\cdot}6H_2O$ content and the Ti content of the Ti@Ce substrate.

Characterization: The crystal structure of all samples was characterized by using an X-ray powder diffractometer (XRD) with Cu K_α radiation (Bruker D2 PHASER XE-T XRD). The X-ray absorption measurement was carried at the National Synchrotron Radiation Research Center (NSRRC), Taiwan. Ce L_3-edge and Ti K-edge were performed at a DCM tender X-ray beamline 16 A with energy resolution set to 0.25 eV. The optical properties, including UV–vis and photoluminescence spectra, were measured by UV– vis/NIR spectrophotometer (Jasco V-670) and Jasco FP-6300 spectrofluorometer. The morphologies and elemental mapping were studied using transmission electron microscopy (TEM) with an accelerating voltage of 200 keV (FEI Tecnai G2 F-20 S-TWIN, FEI Talos F200XG2). The STEM-EELS was done with a Nion STEM microscope operated at 100 keV.

Photocatalytic Activity: Methylene blue (MB) with concentration 10^{-5} m was used to evaluate the photocatalyst performance of CeO_2 NPs, and TiO_2@H-CeO_2 composite after reacting with Cerium (III) nitrate hexahydrate with different concentrations. The samples (50 mg) were mixed with MB solution (50 mL), stirred for 30 min in dark conditions, and then illuminated with UV or visible light. For UV light irradiation, a 400 W mercury lamp with λ_{max} = 365 nm was used as the light source. A 300 W sunlight-simulated lamp with radiation wavelength from 380 to 780 nm was applied for visible light irradiation. Within every 10 min (UV light) or 20 min (visible light), about 3 mL of the mixed solution was taken out and filtered for the absorbance investigation. The absorbance of the MB was measured with a UV–vis/NIR spectrophotometer.

[1] A. Fujishima, K. Honda, *Nature* **1972**, *238*, 37.

[2] G. Divyaa, G. Jaishreea, T. Sivarao, K. V. D. Lakshmi, *RSC Adv.* **2023**, *13*, 8692.

[3] L. Matejová, I. Troppová, Z. Jankovská, H. Sezimová, J. Endres, P.ˇ Peikertová, M. M. G. Leon, *Surf. Interfaces* **2023**, *38*, 102762.

[4] C. Xia, L. Yuan, H. Song, C. Zhang, Z. Li, Y. Zou, J. Li, T. Bao, C. Yu, C. Liu, *Small* **2023**, *19*, 2300292.

[5] M. I. M. Diaz, A. Lecestre, L. Salvagnac, B. Bounor, D. Pech, M. D. Rouhani, A. Esteve, C. Rossi, *Appl. Surf. Sci.* **2022**, *588*, 152919. [6] X. Wang, H. Xu, X. Luo, M. Li, M. Dai, Q. Chen, H. Song, *Colloid Interface Sci. Commun.* **2021**, *44*, 100476.

[7] Q. Du, J. Ma, X. Shao, W. Wang, G. Tian, *Chem. Phys. Lett.* **2019**, *714*, 208.

[8] M. M. Rhaman, S. Ganguli, S. Bera, S. Bahadur Rawal, A. K.
Chakraborty, *J. Water Process. Eng.* **2020**, *36*, 101256.

[9] F. Lu, K. Chen, Q. Fang, H. Cai, D. Ma, D. Wang, X. Li, C. Zuo, S. Wang, *J. Environ. Chem. Eng.* **2021**, *9*, 105840.

[10] I. Kitsou, P. Panagopoulos, T. h. Maggos, M. Arkas, A. Tsetsekou, *Appl. Surf. Sci.* **2018**, *441*, 223.

[11] J. W. Lee, M. R. Othman, Y. Eom, T. G. Lee, W. S. Kim, J. Kim, *Microporous Mesoporous Mater.* **2018**, *116*, 561.

[12] L. Wu, Y. Zhou, W. Nie, L. Song, P. Chen, *Appl. Surf. Sci.* **2015**, *351*, 320.
[13] B. Trouiller, R. Reliene, A. Westbrook, P. Solaimani, R. H. Schiestl, *Cancer Res.* **2009**, *69*, 8784.
[14] J. Cai, X. Wu, S. Li, F. Zheng, *Appl. Catal. B* **2017**, *201*, 12.
[15] S. Soltani, N. Khanian, U. Rashid, T. S. Y. Choong, *Renewable Energy* **2020**, *151*, 1076.
[16] X. Zheng, X. Li, H. Peng, J. Wen, *J. Phys. Chem. Solids* **2018**, *123*, 206.
[17] Z. Cao, X. Chen, L. Xing, Y. Liao, M. Xu, X. Li, X. Liu, W. Li, *J. Power Sources* **2018**, *379*, 174.
[18] X. Liu, K. Zhou, L. Wang, B. Wang, Y. Li, *J. Am. Chem. Soc.* **2009**, *131*, 3140.
[19] R. Kumar Mandal, S. Kumar Pradhan, *Mater. Today: Proc.* **2022**, *66*, 3307.
[20] H. Jiang, M. Li, J. Liu, X. Li, L. Tian, P. Chen, *Ceram. Int.* **2018**, *44*, 2709.
[21] X. Qu, D. Xie, L. Gao, F. Du, *Mater. Sci. Semicond. Process.* **2014**, *26*, 657.
[22] V. Kamari, A. Sharma, N. Kumar, M. Sillanpää, P. R. Makgwane, M. Ahmaruzzaman, A. Hosseini-Bandegharaei, M. Rani, P. Chinnumuthu, *Inorg. Chem. Commun.* **2023**, *151*, 110564.
[23] Y. Wang, J. Zhao, T. Wang, Y. Li, X. Li, J. Yin, C. Wang, *J. Catal.* **2016**, *337*, 293.
[24] Y. C. Chen, Y. C. Chang, A. Gloter, P. K. Hsu, J. M. Song, S. Y. Chen, *Appl. Surf. Sci.* **2021**, *566*, 150602.
[25] C. Albertoni, I. Barroso-Martín, A. Infantes-Molina, E. RodríguezCastellón, A. Talon, H. Zhao, S. You, A. Vomiero, E. Moretti, *Mater. Chem. Front.* **2021**, *5*, 4138.
[26] M. Mahamud, A. M. Taddesse, Y. Bogale, Z. Bezu, *Mater. Res. Bull.* **2023**, *161*, 112176.
[27] L. T. T. Tuyen, D. A. Quang, T. T. T. Toan, T. Q. Tung, T. T. Hoa, T. X. Mau, D. Q. Khieu, *J. Environ. Chem. Eng.* **2018**, *6*, 5999.
[28] B. Yuan, Y. Long, L. Wu, K. Liang, H. Wen, S. Luo, H. Huo, H. Yang, J. Ma, *Catal. Sci. Technol.* **2016**, *6*, 6396.
[29] F. B. Li, X. Z. Li, *Appl. Catal., A* **2002**, *228*, 15.
[30] N. Serpone, D. Lawless, R. Khairutdinov, *J. Phys. Chem.* **1995**, *99*, 16646.
[31] Q. Xiang, K. Lv, J. Yu, *Appl. Catal., B* **2010**, *96*, 557.
[32] D. Cabaret, A. Bordage, A. Juhin, M. Arfaoui, E. Gaudry, *Phys. Chem.*
Chem. Phys. **2010**, *12*, 5619.
[33] F. Farges, G. E. Brown, Jr., J. J. Rehr, *Phys. Rev. B* **1997**, *56*, 1809.
[34] T. Uozumi, K. Okada, A. Kotani, O. Durmeyer, J. P. Kappler, E. Beaurepaire, J. C. Parlebas, *Europhys. Lett.* **1992**, *18*, 85.
[35] Z. Y. Wu, G. Ouvrard, P. Gressier, C. R. Natoli, *Phys. Rev. B* **1997**, *55*, 10382.
[36] P. L. Fèvre, H. Magnan, D. Chandesris, J. Jupille, S. Bourgeois, A. Barbier, W. Drube, T. Uozumi, A. Kotani, *Nucl. Instrum. Methods Phys.*
Res., Sect. B **2005**, *547*, 176.
[37] V. Luca, S. Djajanti, R. F. Howe, *J. Phys. Chem. B* **1998**, *102*, 10650.
[38] C. Yogi, K. Kojima, T. Hashishin, N. Wada, Y. Inada, E. D. Gaspera, M. Bersani, A. Martucci, L. Liu, T. K. Sham, *J. Phys. Chem. C* **2011**, *115*, 6554.
[39] K. Ozawa, M. Emori, S. Yamamoto, R. Yukawa, S. Yamamoto, R. Hobara, K. Fujikawa, H. Sakama, I. Matsuda, *J. Phys. Chem. Lett.* **2014**, *5*, 1953.
[40] B. Choudhury, B. Borah, A. Choudhury, *Photochem. Photobiol.* **2012**, *88*, 257.
[41] E. N. Tseng, Y. T. Hsiao, Y. C. Chen, S. Y. Chen, A. Gloter, J. M. Song, *Nanoscale* **2019**, *11*, 3574.